TECHNICAL ARTICLE



Functional Fatigue of NiTi Shape Memory Alloy: Effect of Loading Frequency and Source of Residual Strains

R. Sidharth¹ · A. S. K. Mohammed¹ · H. Sehitoglu¹

Received: 8 August 2022/Revised: 7 October 2022/Accepted: 13 October 2022/Published online: 16 November 2022 © ASM International 2022

Abstract Due to latent heat release and the consequent thermomechanical coupling, NiTi SMAs are highly rate sensitive. In this study, the effect of loading frequency on the functional characteristics of superelastic NiTi is explored under fatigue loading. The variation and interplay between the elastocaloric temperature change, forward/reverse transformation stresses, residual strain accumulation and hysteresis were studied for single crystals compressed along the $\langle 011 \rangle$ and $\langle 001 \rangle$ loading orientation. It is shown that the functionality of NiTi is better at higher loading frequency due to reduced hysteresis and the functional degradation is linked to transformation induced plasticity in the austenitic domains. TEM investigation reveals transformation induced parallel dislocations not only on the widely reported $\langle 100 \rangle \{011\}_{B2}$ slip system but also on the $\langle 1\overline{1}1\rangle \{011\}_{\rm B2}$ slip system. The source of these dislocations is traced to the type II and type I internal twins of the martensite correspondent variant pair (CVP) via lattice correspondence, respectively. Moreover, it was observed that these dislocations pile-up at the precipitate-B2 interface and activate slip and/or shear into the precipitates. This is yet another functional degradation and dissipative mechanism that has not been reported before.

This invited article is part of a special issue of Shape Memory and Superelasticity honoring Etienne Patoor for his contributions to the field of phase transforming materials and shape memory alloys. The special issue was organized by Dr. Fodil Meraghni, Ecole Nationale Supérieure d'Arts et Métiers (Arts et Métiers Institute of Technology), and Dr. Dimitris Lagoudas, Texas A&M University.

☑ R. Sidharth ravi8@illinois.edu

Department of Mechanical Science and Engineering, University of Illinois, Urbana, IL 61801, USA



Keywords Functional fatigue · Superelasticity · Internal twins · Dislocations · Martensite

Introduction

NiTi is one of the most successful shape memory alloys (SMA) of today. Its unique functional properties enable them to be employed in wide range of engineering applications such as biomedical stents, active/passive damping of vibrations, solid state actuators and elastocaloric cooling, to name a few [1-6]. Under the right temperature condition, an austenitic to martensitic phase transformation, resulting in large strain accommodation, can be achieved by the application of an external load. Reversal of this phase transformation by unloading (superelastic effect) or unloading followed by heating (shape memory effect) recovers almost all the strain. The unrecoverable strain accumulates with cycling. This transformation induced plasticity is one of the mechanisms of energy dissipation in a superelastic deformation and contributes to the total hysteresis.

The superelastic hysteresis is highly sensitive to the loading rate. Effect of loading frequency on the mechanical response of NiTi was clearly established in our previous work [7]. By comparing NiTi with a starkly contrasting SMA FeMnAlNi, which exhibits a large superelastic window of operation (> 400 °C) [8], it was shown that the frequency sensitivity of SMAs is related to the Clausius-Clapeyron slope. At the atomic scale, the frictional resistance to the motion of the A-M interface dictates frequency dependence of superelastic hysteresis. The self-heating brought about by the latent heat release during the austenite to martensite transformation maximizes the difference in the chemical contribution to the Gibbs free energy [9, 10],

increases the resistance of the A-M interface and causes hardening during the forward transformation. Whereas the associated temperature rise stabilizes austenite, provides an additional driving force, and increases the mobility of the interface during reverse transformation upon unloading, effectively reducing the total hysteretic area. On the other hand, the frictional resistance of the martensite twin interface of the internally twinned martensite is less sensitive to temperature as this interface is not associated with two different phases. Its mobility depends more on the burgers vector of the twin partials, elastic modulus of martensite and the peierls stress in the martensite [6, 11]. Figure 1 schematically shows the different contributions to the superelastic hysteresis. As shown, the contribution for the total hysteresis comes from (i) the transitory part, which is takes into account the energy dissipated due to the motion of the A-M interface and it changes with loading frequency (Fig. 1a), (ii) the phase transformation part, which takes into consideration the energy dissipated due to the transformation induced defects/dislocations (Fig. 1b) and (iii) the intrinsic part, which considers the energy dissipated via the motion of the internal twin interfaces of the martensite (Fig. 1c).

Frequency sensitivity of SMAs has been extensively studied for a single load/unload cycle [12–23]. Plastic dissipation, which constitutes the phase transformation part of the hysteresis, during a superelastic load/unload cycle dictates functional fatigue performance. On the other hand, the structural fatigue lifetime of SMAs correlates with the total hysteretic area of the stress–strain curve [24] which is affected by both loading frequency and plastic dissipation (Fig. 1a, b). It was observed that the fatigue lifetime decreases with increasing loading frequency [25, 26] even though the total normalized hysteresis (specific damping

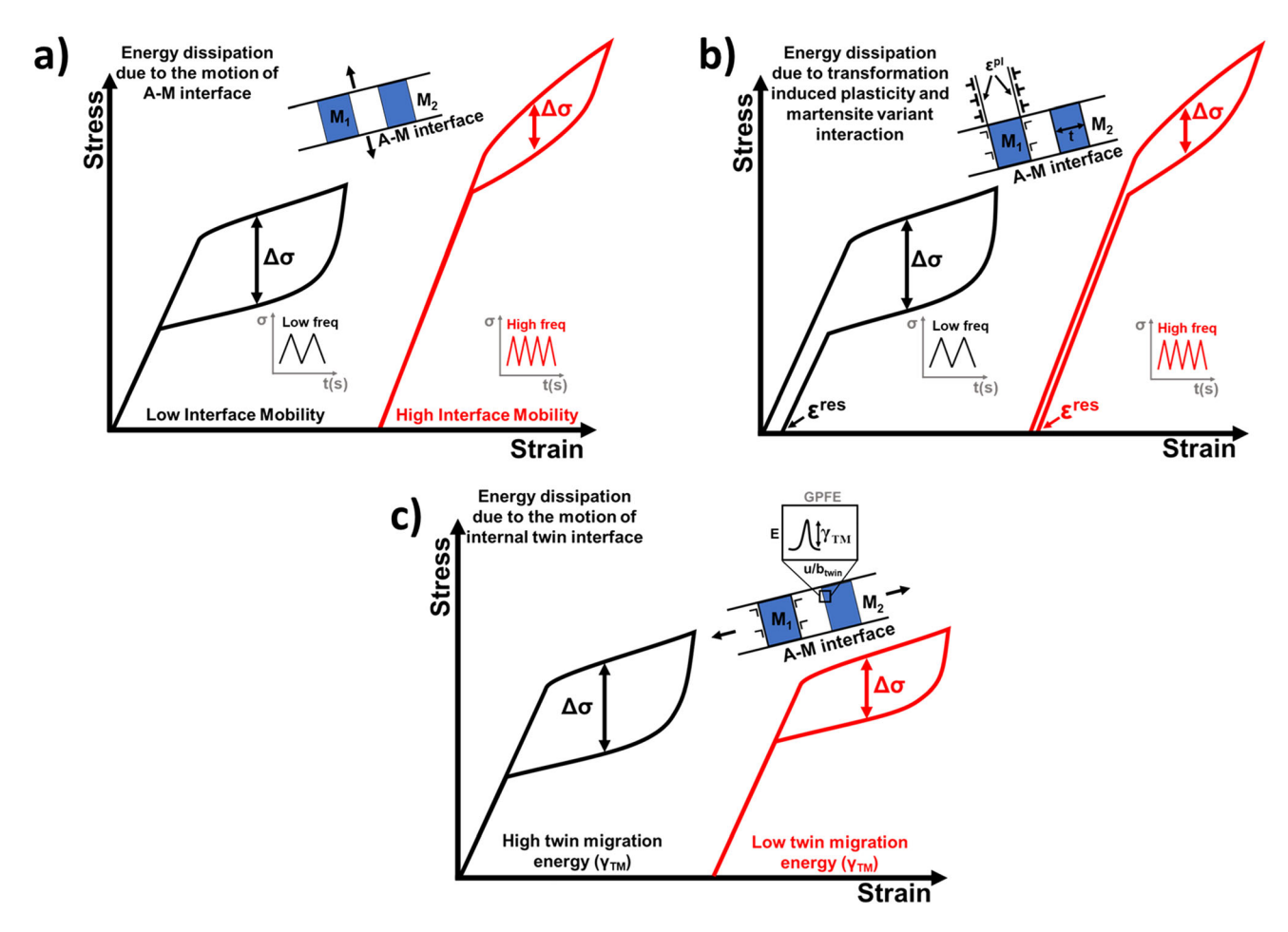


Fig. 1 Contributions to the total hysteresis of a superelastic deformation. **a** The transitory part considers the energy dissipation due to frictional resistance of the A-M interface. Hysteresis increases with increased frictional resistance. **b** The phase transformation part considers energy dissipation due to the stress-induced martensitic phase transformation and the associated transformation induced plasticity at the A-M interface. Hysteresis increases with increased

plastic dissipation and martensite variant interaction. \mathbf{c} The intrinsic part considers the energy dissipation intrinsic to the austenite and martensite phases, respectively. Intrinsic part is dominated by the energy dissipation due to twin boundary motion of the internally twinned martensite and the hysteresis increases with increased twin migration energy

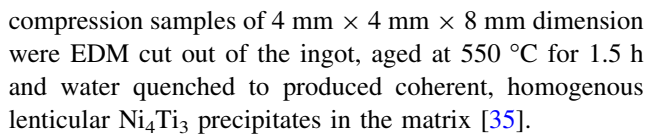


capacity) decreases (Fig. 1a, b). It was argued that the increase in the stress levels at higher loading frequency accelerates crack nucleation. However, it is known that crack initiation is governed by evolution of strain energy, which not only depends on the local stress field but also on the residual strain accumulated within localized regions [27–29]. Moreover, in our previous work, we established the relationship between the mechanisms behind functional fatigue and structural fatigue in SMAs by demonstrating that structural failure by crack initiation and growth occurs along A-M interface [30, 31] and makes it the weakest link in the microstructure. Experiments [32–42] and modeling efforts [37, 39, 43-45] have explicitly shown the role played by the A-M interface and the internal twin interfaces of the martensite in transformation induced plastic dissipation in diverse SMAs. Dislocation creation in austenitic domains in the vicinity of a moving A-M interface gives rise to residual strain accumulation, pin the A-M interface and stabilize martensite at zero stress thereby influencing functional degradation (i.e. functional fatigue) [36, 46–49]. Ultimately crack initiation and growth (i.e. structural fatigue) occurs along the A-M interface [30, 31]. Thereby, understanding the interplay between loading frequency, residual strain accumulation and plastic dissipation is crucial for predictive modeling of functional and structural fatigue of SMAs.

To this end, the current study focuses on the functional fatigue of NiTi single crystals subjected to compressive cyclic loading for various loading frequencies. The frequency range is chosen as 0.01-10 Hz, covering low frequency quasi-static test regimes to higher frequencies expected in practical applications such as vibration damping in space structures and earthquake resistant buildings [50-52]. Single crystals with $\langle 011 \rangle$ and (001) loading orientation are employed to eliminate grain boundary effects and provide clear insight into the active mechanisms. High-speed optical and infrared cameras are used to capture in situ images during deformation for digital image correlation and temperature measurement, respectively. Both non-contact methods serve as essential tools to accurately map the spatial evolution of strain and temperature. Post-mortem TEM analysis is carried out to the source of residual accurately pinpoint strain accumulation.

Materials and Methods

In this study $Ni_{50.8}$ Ti (at.%) $\langle 011 \rangle$ and $\langle 001 \rangle$ single crystals were used. The single crystals were grown using Bridgeman technique in an inert environment. $Ni_{50.8}$ Ti single crystal ingots were solutionized at 920 °C for 24 h in an inert atmosphere and water quenched. Then miniature



Prior to loading, all samples were mechanically polished with abrasive papers up to P4000 and finished with 1 μm suspended alumina to achieve mirror surface finish. 600 grit SiC powder was air blasted on the mirror surface to obtain speckle pattern for full-field strain measurements using DIC. On the back side, the surface was coarse ground with P400 abrasive paper and airbrushed with black paint to achieve high emissivity for IR thermography. Functional fatigue experiments in compression were performed on an Instron servo hydraulic load frame under displacement control at different loading rates ranging from 0.01 to 10 Hz. The images for DIC were taken by an FLIR-ORX-10G-51S5M high speed camera operating in the range of 1fps for low frequency test to 500 fps for the high frequency test. The corresponding spatial resolution of the images was of the order of 3 µm/pixel. The DIC strain field within this area of interest was determined using a commercial software VIC-2D by correlated solutions. For IR thermography, FLIR A6753 IR camera was used at frame rates of 25 fps to 394 fps for low frequency and high frequency tests, respectively. The IR camera was calibrated for a temperature range of 10 °C to 90 °C. All the experiments were performed at room temperature. Dual camera setup shown in the prior study [7] was employed to obtain images for DIC and IR thermography simultaneously.

For the TEM analysis, lamella was prepared via focused ion beam milling on the Thermo Scios2 dual beam SEM/FIB. The crystallographic orientation of the bulk sample was confirmed via electron backscattered diffraction (EBSD) and the sample was rotated appropriately to mill a lamella with the preferred zone axis for a thorough dislocation analysis. TEM analysis was carried out in JOEL 2100 Cryo TEM operated under 200 kV accelerating voltage. Double tilt holder was utilized to achieve on-zone and two-beam conditions for accurately pinpointing the activated slip systems.

Results

NiTi (011)

Cycle 1 stress strain loops are presented in Fig. 2 for all the loading frequencies. The maximum applied strains were maintained between 1.8 and 2.1% to minimize amplitude effects. The hysteresis decreases with increasing loading frequency, whereas the 0.1% strain-offset transformation stress increases. Sample exhibits considerable hardening during transformation, which can be attributed to the self-



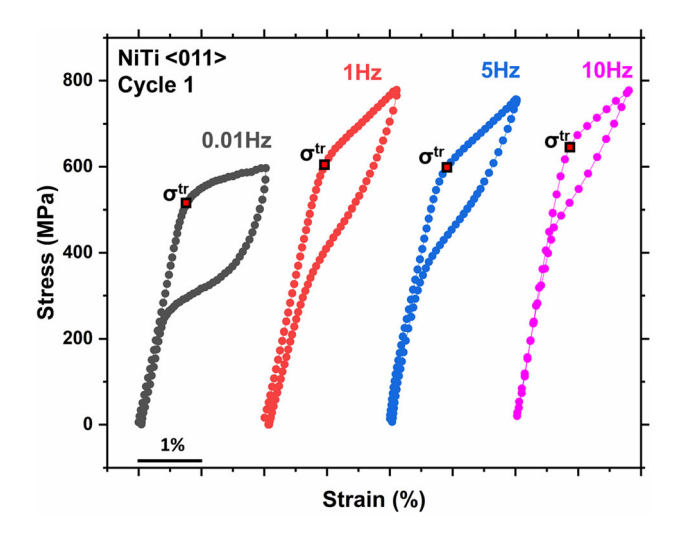


Fig. 2 NiTi $\langle 011 \rangle$ stress strain loops for different loading frequencies. Note the increase in 0.1% strain offset transformation stress and decrease in hysteresis with frequency

heating during loading. Functional fatigue results for NiTi $\langle 011 \rangle$ single crystals are shown in Fig. 3. For the sake of brevity only the 0.01 Hz and 10 Hz results are shown. The maximum applied strain was kept at 1.8 to 2.1%. Note that the hysteresis decreases with increasing loading frequency. Upon continued cycling, residual strain accumulates, and the stress-strain behavior approaches a stable state after cycle 10. This is also reflected in the temperature variation of the entire sample shown in Fig. 3. The maximum temperature, which signifies the end of loading and the end of forward transformation, and the minimum temperature, which signifies the end of reverse transformation, approach a stable state after cycle 10. The DIC contours presented in Fig. 3 show that the residual strain domains at the end of cycle 10 coincides, spatially, with the location of maximum strain at the peak load. This suggests that residual strain accumulation is linked to the martensitic transformation.

Figure 4 depicts the variation of local temperature with time for 1 Hz loading frequency. A representative local area of interest (AOI) is shown in the insets of Figs. 5 and 9. One can note that the magnitude of temperature rise in the forward transformation is smaller than the temperature decrease during the reverse transformation. This asymmetry in the temperature variation with respect to forward/reverse transformation is more pronounced in the lower loading frequencies and approaches a symmetric behavior as the frequency is increased. This aspect was addressed in our previous work and was attributed to the dissimilarity in the latent heat released/absorbed during forward/reverse transformations, respectively [7]. As shown in Fig. 4, various temperature quantities were extracted for further analysis. One of them is the variation of the total reversible

temperature change ($\Delta T_{\rm rev}$) with cycling. $\Delta T_{\rm rev}$ was calculated as the difference between the measured maximum temperature and minimum temperature per cycle and presented in Fig. 5 for all loading frequencies. The temperature is maximum at the end of loading and minimum at the end of reverse transformation during unloading [7]. It is evident that $\Delta T_{\rm rev}$ decreases drastically and stabilizes after cycle 10 for all the loading frequencies. One should note that $\Delta T_{\rm rev}$ scales with the total volume of transformation. Total volume of transformation decreases every cycle and stabilizes after cycle 10. So does $\Delta T_{\rm rev}$. One can also note that $\Delta T_{\rm rev}$ increases with frequency due to reduced heat transfer into the ambient environment within the time frame of the test.

The stress-temperature response is depicted in Fig. 6. The 0.1% strain-offset transformation stress extracted for each loading frequency is presented in Fig. 6c for cycle 1 and 10. It is evident that transformation stress increases with loading frequency and decreases with cycling. To rationalize the increase in transformation stress with loading frequency, $\Delta T_{\rm tr}$ at 0.1% strain-offset transformation stress was extracted for cycles 1 and 10. $\Delta T_{\rm tr}$ increases with loading frequency and decreases with cycling. These results suggest that transformation begins, at the microscale, in the elastic regime of the stress-strain curve and produces a measurable temperature change to influence the 0.1% strain-offset transformation stress due to the Clausius-Clapeyron effect. However, looking at the transformation stress after 10 loading cycles, there is a considerable decrease which can be attributed to two contributions: (i) the decrease in $\Delta T_{\rm tr}$ and (ii) the internal stress field generated by residual dislocations assisting transformation. See the discussion "Effect of Loading Frequency on Transformation Stress" and "Effect of Cycling on Transformation Stress and Hysteresis" sections for more details.

NiTi $\langle 001 \rangle$

Cycle 1 stress strain loops for the $\langle 001 \rangle$ loading orientation are presented in Fig. 7 for all the loading frequencies. The maximum applied strains were maintained between 2 and 2.3% to minimize amplitude effects. It is evident that the hysteresis decreases with increasing loading frequency, whereas the 0.1% transformation stress increases. Sample exhibits considerable hardening during transformation, which can be attributed to the self-heating during loading. Functional fatigue results presented in Fig. 8 demonstrate that there is no residual strain accumulation for this orientation. As a result, the stress–strain loops and the corresponding temperature variation shown in Fig. 8 remain stable for all the applied 20 cycles. DIC contour plots



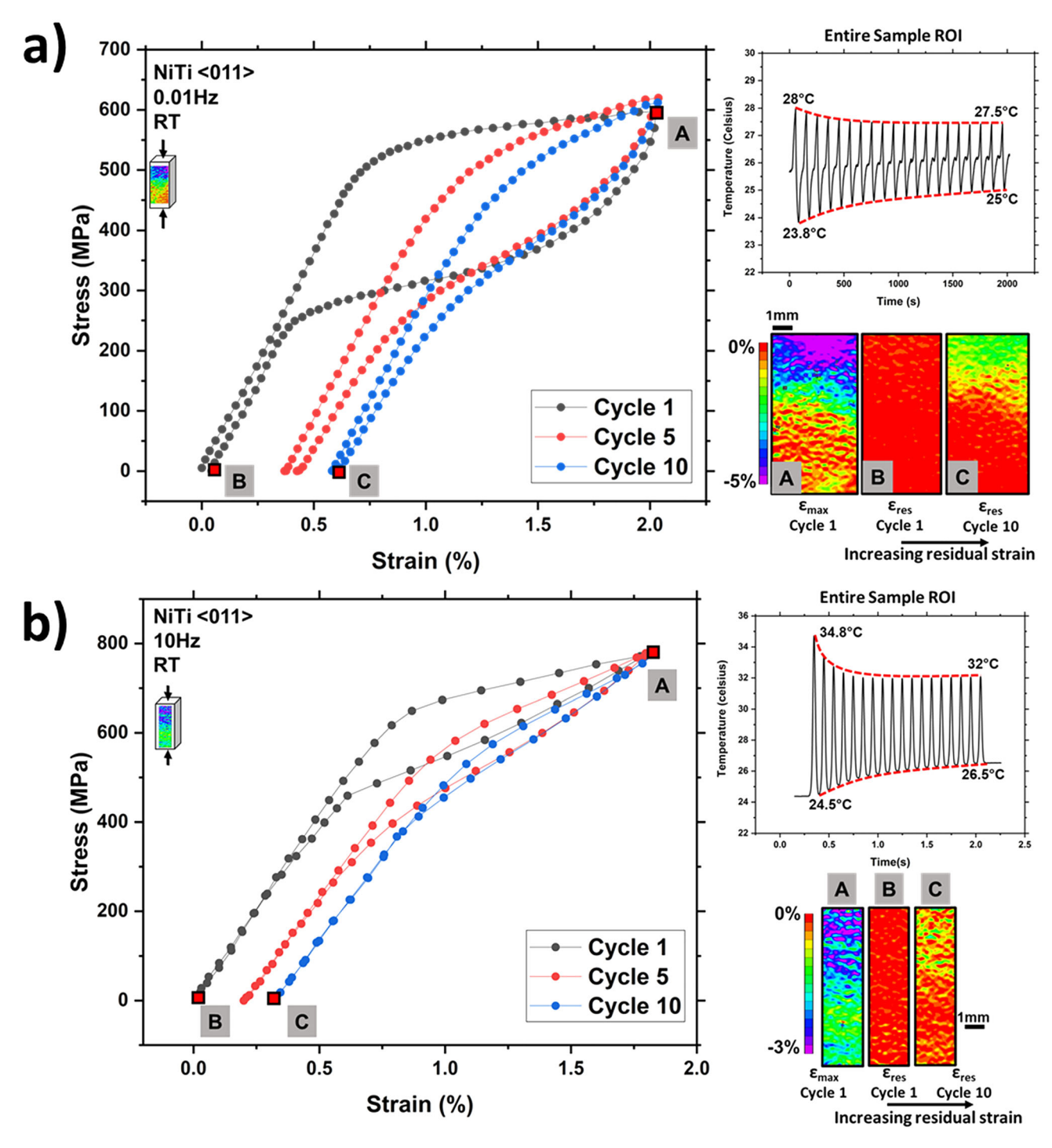


Fig. 3 Functional fatigue of NiTi $\langle 011 \rangle$ in compression for **a** 0.01 Hz and **b** 10 Hz loading frequency. Compared to 0.01 Hz, note the decrease in hysteresis and accumulated residual strain for 10 Hz loading frequency. Point 'A' depicts the maximum strain contour for

cycle 1 whereas points 'B' and 'C' depict the residual strain contours for cycle 1 and 10, respectively. Note the variation in temperature averaged over the entire sample

validate that the unloaded microstructure is devoid of residual strain.

For the low frequency loading of 0.01 Hz, the mean temperature of the entire sample goes down by 0.8 °C at the end of 20 cycles whereas for the maximum frequency

of 10 Hz the mean temperature goes up by 0.9 °C, which is attributed to the asymmetry in ΔT during loading and unloading for the lower frequencies [7]. However, if cycling were continued for longer duration, heat transfer with the ambient environment would influence the



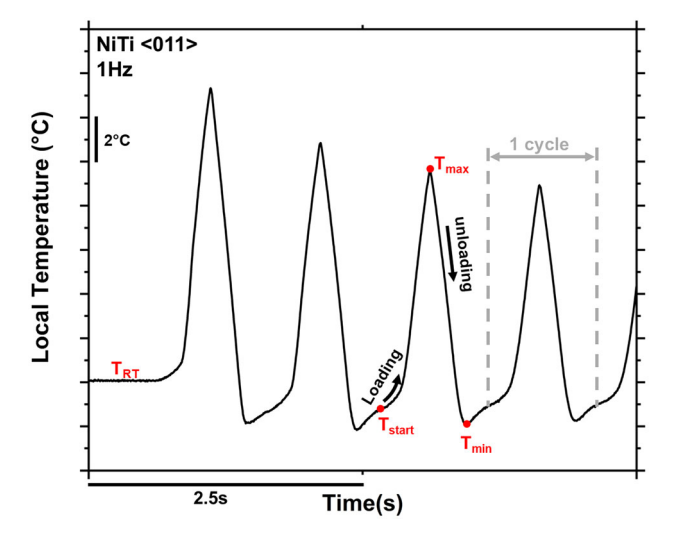


Fig. 4 Variation in the local temperature of a representative sample with respect to time for 1 Hz loading frequency. A local AOI similar to the ones shown in inset of Figs. 5 and 9 was used to extract the temperature measurement. Various temperature quantities like maximum temperature $(T_{\rm max})$, minimum temperature $(T_{\rm min})$, temperature at start of the loading cycle $(T_{\rm start})$ and temperature at the start of transformation $(T_{\rm tr})$ were extracted from these curves for all the loading frequency

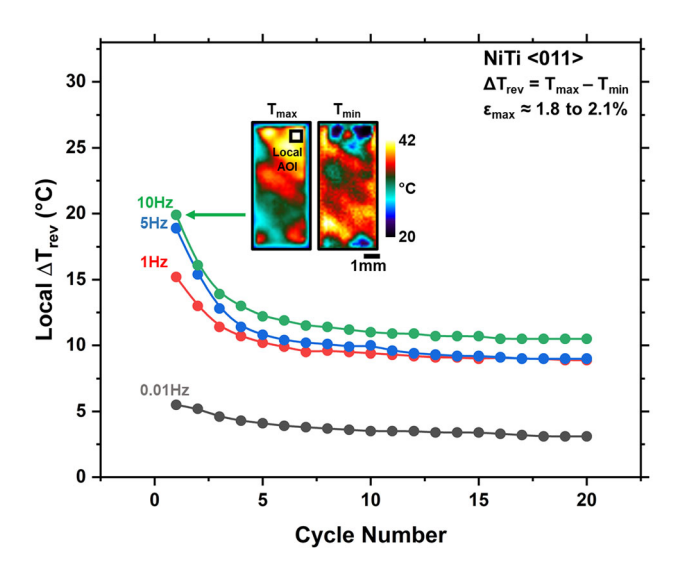


Fig. 5 Variation in the local reversible temperature change with respect to cycle number for NiTi $\langle 011 \rangle$. It is calculated as the difference between the measured maximum temperature, which marks the end of loading, and the minimum temperature, which marks the end of reverse transformation. This directly correlates with the volume of transformed material. Inset features the IR micrograph. Note the spatial inhomogeneity in the temperature of the sample which is due to the spatial inhomogeneity in the transformation (seen DIC plots shown in Fig. 3). Temperature was extracted from a 400 $\mu m \times 400~\mu m$ local AOI as shown

minimum, maximum and mean sample temperature to stabilize. Just as shown in Fig. 4, various temperature quantities were extracted for NiTi $\langle 001 \rangle$ as well. $\Delta T_{\rm rev}$ for

all the loading frequencies are shown in Fig. 9. It displays a stable behavior with cycling since the transformation volume and the corresponding reversible strains remain unchanged.

The stress-temperature response is shown in Fig. 10. The 0.1% transformation stress marked in Fig. 7 was used to determine temperature change at transformation. Just like the transformation stress (Fig. 10), $\Delta T_{\rm tr}$ follows an increasing trend as well (Fig. 10b). As discussed in the previous section, this temperature change is brought about by the latent heat release as the martensitic transformation nucleates in a microscopic domain during the elastic portion of the stress–strain curve. However, both the transformation stress and $\Delta T_{\rm tr}$ remain unchanged with cycling due to a stable mechanical response reinforcing the role played by residual strain in modulating the transformation stress.

Residual Strains and Hysteresis with Cycling

Hysteresis, in terms of normalized dissipated energy (specific damping capacity), was extracted for NiTi 001 and $\langle 011 \rangle$. As seen in Fig. 11a, hysteresis decreases with loading frequency for both $\langle 001 \rangle$ and $\langle 011 \rangle$. One reason for this is the decrease in the frictional resistance of the A-M interface (transitory contribution). The temperature rise during forward transformation provides an additional driving force and increases the mobility of the A-M interface during reverse transformation. This was demonstrated using a thermomechanical model adapted from [9, 10, 35] and modified to take the experimentally measured temperature change as an input. On the other hand, as the $\langle 011 \rangle$ samples are functionally fatigued for 20 cycles, the residual strain accumulation is lower for higher frequencies (Fig. 11b, c). This suggests that, for the $\langle 011 \rangle$ loading orientation, the hysteretic contribution from transformation induced plasticity is reducing as the loading frequency is increased. The normalized dissipated energy for $\langle 011 \rangle$ at cycle 10 overlaps with that of $\langle 001 \rangle$. At this point, it is worth noting that the lower specific damping capacity for (001) pertains to the absence of plastic dissipation as depicted in Figs. 8, 11a and b. The reduction in hysteresis due to enhanced mobility of the A-M interface (Transitory part) influences the energy dissipation due to the transformation induced plasticity (phase transformation part). This can be validated by tracking the residual strain accumulation in NiTi (011) upon cycling. As shown in Fig. 11b and c, the residual strain accumulation is systematically lower as the frequency is increased. As the residual strains saturate after cycle 10, the specific damping capacity of NiTi (011) overlaps with that of NiTi (001) suggesting that contribution to the hysteresis from transformation induced plasticity is approaching zero.



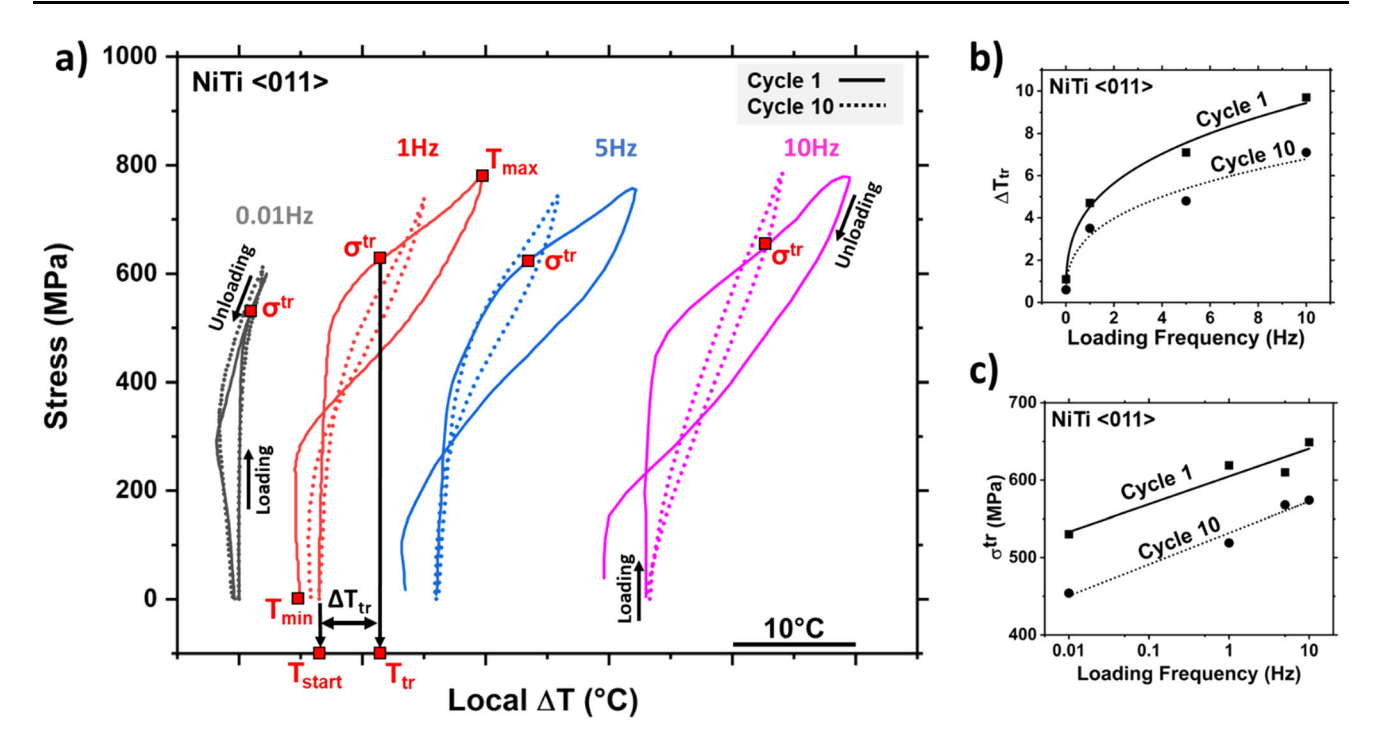


Fig. 6 a Stress (vs) Local temperature change (ΔT) for cycle 1 and 10 for NiTi $\langle 011 \rangle$. Local ΔT for each cycle was calculated as the difference between temperature at any point during loading/unloading and $T_{\rm start}$. The 0.1% strain-offset transformation stress extracted from the stress–strain curve is marked in red. **b** The variation in temperature change at transformation ($\Delta T_{\rm tr}$) with respect to loading

frequency for cycle 1 and 10. $\Delta T_{\rm tr}$ was calculated as the difference between the temperature at the start of loading ($T_{\rm start}$) and the temperature at 0.1% transformation ($T_{\rm tr}$). c The variation in 0.1% transformation stress with respect to loading frequency for cycle 1 and 10 (Color figure online)

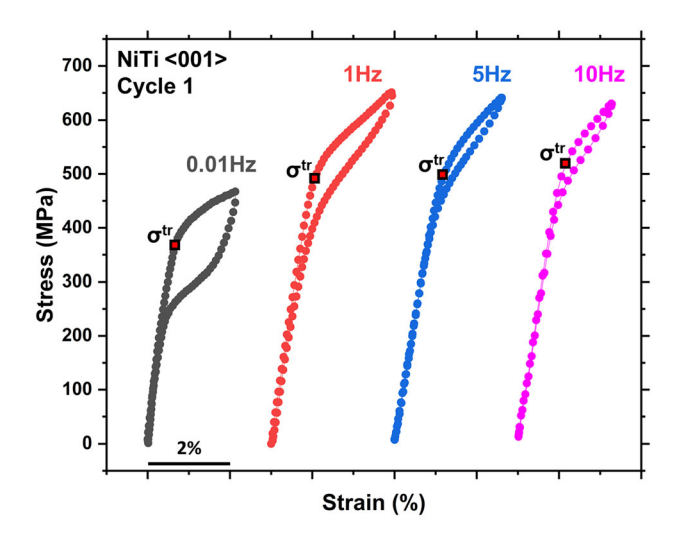


Fig. 7 NiTi $\langle 001 \rangle$ stress strain loops for different loading frequencies. Note the increase in 0.1% strain offset transformation stress and decrease in hysteresis with frequency

Discussion

This study has clearly demonstrated the coupling between loading frequency and functional fatigue of NiTi SMA. Just by comparing the two different orientations $\langle 011 \rangle$ and $\langle 001 \rangle$, conclusive evidence can be drawn towards

common underlying mechanisms that influence the functional response such as the hysteresis, temperature evolution, transformation stress and residual strain accumulation. The results demonstrate the following: (i) normalized hysteresis decreases with loading frequency for both the orientations, (ii) transformation stress increases with loading frequency for both the orientations, (iii) transformation stress decreases with cycling for (011) whereas it stays the same for $\langle 001 \rangle$, (iv) normalized hysteresis is lower for $\langle 001 \rangle$ compared to that of $\langle 011 \rangle$, (v) upon cycling the normalized hysteresis for (011) decreases and stabilizes at the value of $\langle 001 \rangle$ after cycle 10 and (vi) synchronously the residual strain accumulation stabilizes for (011) after cycle 10 whereas there is no residual strain accumulation for (001). The pertinent mechanisms behind these experimental findings are further discussed below.

Effect of Loading Frequency on Transformation Stress

The effect of loading frequency on the hysteresis was thoroughly discussed in our previous work [7]. The amplified self-heating of the sample with increased loading frequency rises the stress levels of forward and reverse



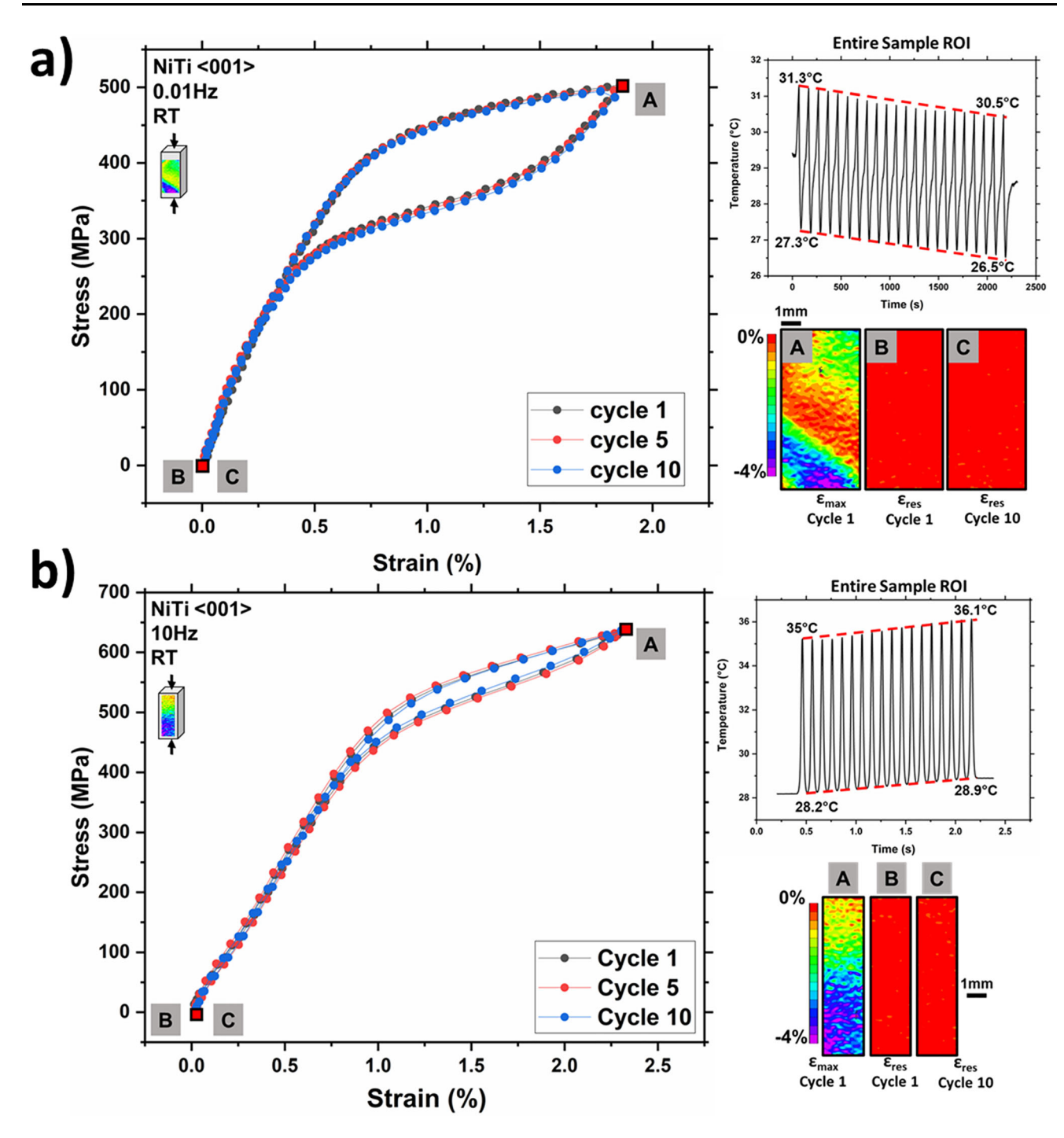


Fig. 8 Functional fatigue of NiTi $\langle 001 \rangle$ in compression for a 0.01 Hz and **b** 10 Hz loading frequency. Compared to 0.01 Hz, note the decrease in hysteresis for 10 Hz loading frequency. However, there is no residual strain accumulation for both the loading frequencies. Point

'A' depicts the maximum strain contour for cycle 1 whereas points 'B' and 'C' depict the residual strain contours for cycle 1 and 10, respectively. Note the variation in temperature averaged over the entire sample

transformation effectively reducing the net hysteretic area in the 0.01–10 Hz frequency range. At this point it should be noted that, below 0.01 Hz loading frequency, hysteresis exhibits a non-monotonic variation [17–19]. Additionally, the self-heating also increases the 0.1% strain-offset transformation stress which marks the deviation from

linearity of the stress–strain curve. Nucleation of stress-induced martensite always begins from a microscopic region within the sample well before the stress–strain curve exhibits non-linearity. This can be verified by looking at the stress vs local ΔT curves in Figs. 6 and 10. In the purely elastic regime there is little to no increase in temperature.



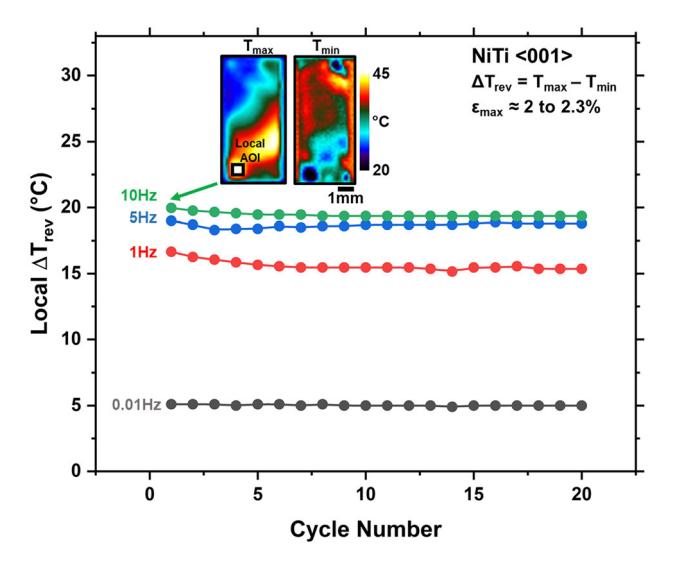


Fig. 9 Variation in the local reversible temperature change with respect to cycle number. It is calculated as the difference between the measured maximum temperature, which marks the end of loading, and the minimum temperature, which marks the end of reverse transformation. This directly correlates with the volume of transformed material. Inset features the IR micrograph. Note the spatial inhomogeneity in the temperature of the sample which is due to the spatial inhomogeneity in the transformation (seen DIC plots shown in Fig. 8). Temperature was extracted from a 400 $\mu m \times 400~\mu m$ local AOI of as shown

However, the local temperature begins to rise at a stress well below the 0.1% strain-offset transformation stress. As the nucleation of martensite commences from a highly localized region, the associated latent heat release rises the temperature of the surrounding material. Thereby, according to the Clausius-Clapeyron relationship, the transformation stress of this surrounding region gets amplified warranting an increase in the externally applied stress to sustain transformation through the surrounding volume of material. Once the volume fraction of martensite reaches a critical value, the stress-strain curve deviates from linearity that generally coincides with the 0.1% strain-offset transformation stress. The temperature change at 0.1% strain-offset transformation stress ($\Delta T_{\rm tr}$) was measured at various loading frequencies for both the loading orientations (Figs. 6b, 10b) and the increase in $\Delta T_{\rm tr}$ with frequency is evident.

Effect of Cycling on Transformation Stress and Hysteresis

Upon functional fatigue, the transformation stress and hysteresis decrease for $\langle 011 \rangle$ whereas it stays the same for $\langle 001 \rangle$ loading orientation. On the other hand, residual

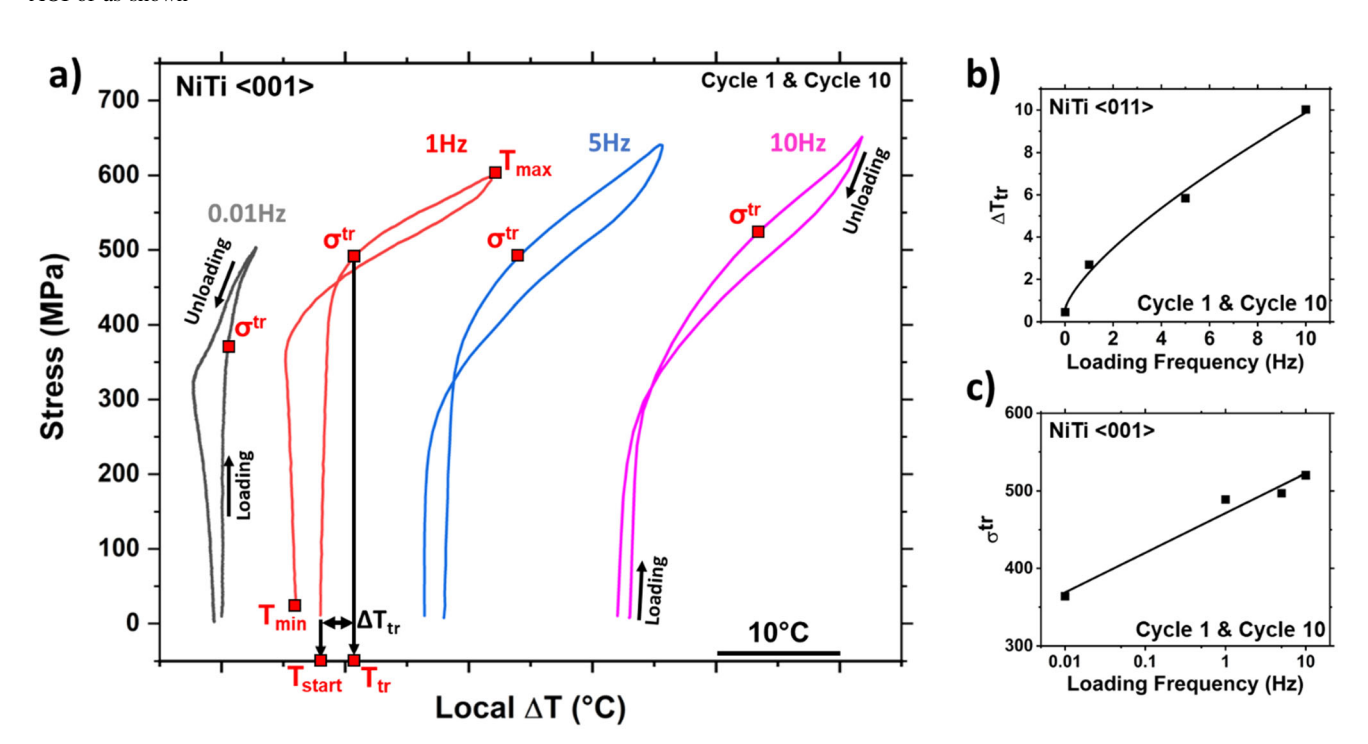


Fig. 10 a Stress (vs) Local temperature change (ΔT) for cycle 1 and 10 for NiTi $\langle 001 \rangle$. Local ΔT for each cycle was calculated as the difference between temperature at any point during loading/unloading and T_{start} . The 0.1% transformation stress extracted from the stress-strain curve is marked in red. The stress vs temperature response displays a stable behavior for all the applied loading cycles. **b** The

variation in temperature change at transformation ($\Delta T_{\rm tr}$) with respect to loading frequency for cycle 1 and 10. $\Delta T_{\rm tr}$ was calculated as the difference between the temperature at the start of loading ($T_{\rm start}$) and the temperature at 0.1% transformation ($T_{\rm tr}$). ${\bf c}$ The variation in 0.1% transformation stress with respect to loading frequency for cycle 1 and 10 (Color figure online)



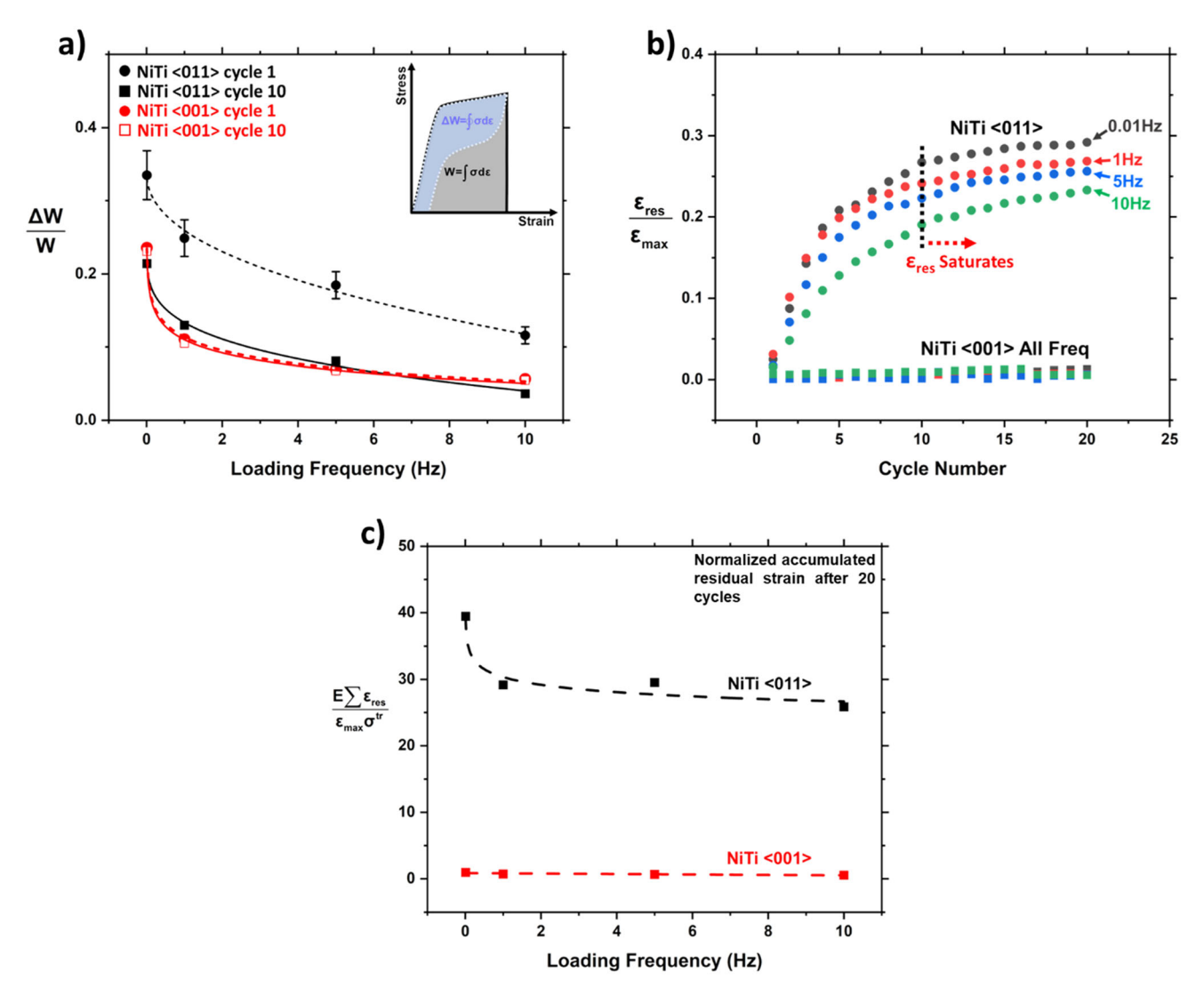


Fig. 11 a Change in normalized hysteresis (specific damping capacity) with respect to loading frequency for NiTi $\langle 011 \rangle$ and $\langle 001 \rangle$ for cycles 1 and 10. **b** Residual strain accumulation with fatigue cycles. **c** Variation in normalized residual strain with loading

frequency. Residual strain is normalized with maximum applied strain (ϵ_{max}) and elastic strains (σ^{tr}/E). Note the decrease in normalized residual strain with respect to loading frequency

strain accumulates for $\langle 011 \rangle$ but not for $\langle 001 \rangle$ due to the generation of transformation induced defects in the microstructure. This conclusively suggests a common underlying mechanism behind residual strain accumulation, transformation stress (both forward and reverse), the overall shape of the hysteresis loop and consequently the dissipated energy. During functional fatigue of $\langle 011 \rangle$, the accumulation of transformation induced defects modulate the stress–strain curve in two ways (i) it generates an internal stress field which assists transformation leading to a decrease in the externally applied stress and (ii) the consequent decrease in the total transformed volume leads to diminishing $\Delta T_{\rm tr}$ and ΔT during loading/unloading meaning a decrease in the stress levels during forward/reverse transformation. For 0.01 Hz loading frequency the

magnitude of change in $\Delta T_{\rm tr}$ and ΔT during loading/unloading is minimal with cycling, therefore the change in $\sigma^{\rm tr}$ and σ during forward/reverse transformation is primarily due to transformation induced defects. As the loading frequency increases $\Delta T_{\rm tr}$ and ΔT during loading/unloading starts affecting the stress levels. Consequently, the shape and the area of the hysteresis loops alter as well. Upon cycling, the hysteretic area reduces gradually indicating a decline in energy dissipated in the form of permanent strains. Ultimately, after 10 cycles, normalized hysteresis for $\langle 011 \rangle$ overlaps with that of $\langle 001 \rangle$ due to a saturation in residual strain accumulation (Fig. 11). The crucial role played by transformation induced defects which gives rise to residual strains and modulates other functional fatigue



characteristics warrants further analysis and the following section is dedicated to that.

Source of Residual Strain During Functional fatigue

TEM Analysis

To uncover the nature of transformation induced defects. TEM analysis was conducted on the $\langle 011 \rangle$ sample cycled 20 times at 0.01 Hz. TEM micrographs (Fig. 12) with zone axis parallel to $[\overline{3}1\overline{1}]$ clearly shows parallel dislocations pertaining to two slip systems. Residual strain accumulates in the form of dislocations that are left behind in the austenite matrix upon unloading. It is known that, in B2 slip systems, can be accommodated on $\{011\}, \{\overline{2}11\}, \{001\}$ slip planes the along $\langle 100 \rangle, \langle 111 \rangle, \langle 011 \rangle$ slip directions, out of which $\langle 100 \rangle \{011\}$ is the most energetically favorable [53]. To establish the slip plane and the burgers vector of these dislocations, another TEM lamella was extracted along the $[1\overline{11}]$ zone axis. Imaging this TEM lamella under different diffraction conditions of $g = \langle 1\overline{10} \rangle$ by appropriately tilting the sample. the corresponding slip plane {110} vanishes. Using the g.b extinction condition, the burgers vector was determined to belong to the $\{011\}$ slip plane and either $\langle 100 \rangle$ or $\langle 1\overline{1}1 \rangle$ slip direction (see Fig. 13). To confirm the slip direction yet another TEM lamella was extracted along the [010] zone axis. Imaging this lamella under $g = [10\overline{1}]$ reveals the clear dislocation contrast (Fig. 14a) and a vanishing condition is reached when imaged under g = [101] (Fig. 14b). This suggests a burgers vector of type (111). However, moving to a different location on the TEM lamella, imaging under the same diffraction conditions of $g = [10\overline{1}]$ (Fig. 15a) and g = [101] dislocations are clearly visible but

imaging under the g = [001] diffraction condition, a vanishing condition is reached suggesting burgers vector of type $\langle 100 \rangle$. The primary difference between these two regions of the TEM lamella is the type of Ni₄Ti₃ variant present in the neighborhood of these dislocations. To understand further, the possible mechanism behind the creation of these dislocations is discussed in the next section.

Mechanism of Dislocation Accumulation During Functional Fatigue

Various studies have attempted to clarify the mechanism behind the source of these elongated parallel dislocations. Such dislocations have been previously observed in the austenitic domains of SMAs which had undergone a martensitic transformation [32, 33, 35, 37–40, 45, 46]. The trace of these dislocations appears to be parallel to the trace of the martensitic twins and therefore suggested to have originated from partial dislocations gliding on the twinning plane. The distortion along the A-M interface should be zero when averaged over large distances but at the scale of the martensitic twins, there exists coherency strains. Additionally, growth/shrinkage of the martensite plate requires coordinated motion of the A-M interface and the internal twin interface. Therefore, Kajiwara [32, 54] proposed that the coherency strains at the A-M interface be accommodated by glide dislocations lying on the twin plane of the martensite to facilitate both compatibility and mobility of the interface. Based on lattice correspondence between B19' martensite and B2 austenite, the martensite twinning shear direction $[01\overline{1}]_{M}$ is parallel to the B2 slip direction [001]_A, the type II martensitic twinning plane $(0.7205 \ 1 \ 1)_{\rm M}$ is nearly parallel to the B2 slip plane $(101)_{\rm A}$ [55–57]. On the other hand, type I martensitic twinning

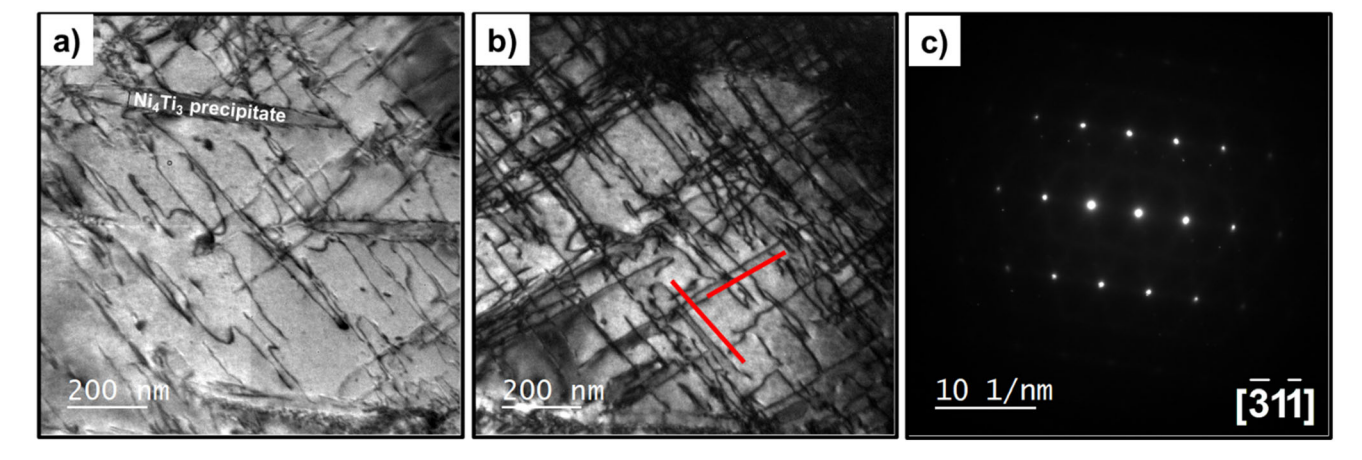


Fig. 12 TEM micrographs of NiTi $\langle 011 \rangle$ sample loaded for 20 cycles at 0.01 Hz imaged along the $[\overline{3}1\overline{1}]$ zone axis. Parallel dislocations belonging to two slip systems are clearly discernable in the bright

field images shown in $\bf a$ and $\bf b$. The corresponding diffraction pattern is shown in $\bf c$. Refer to Figs. 13, 14 and 15 for the burgers vector analysis of these dislocations



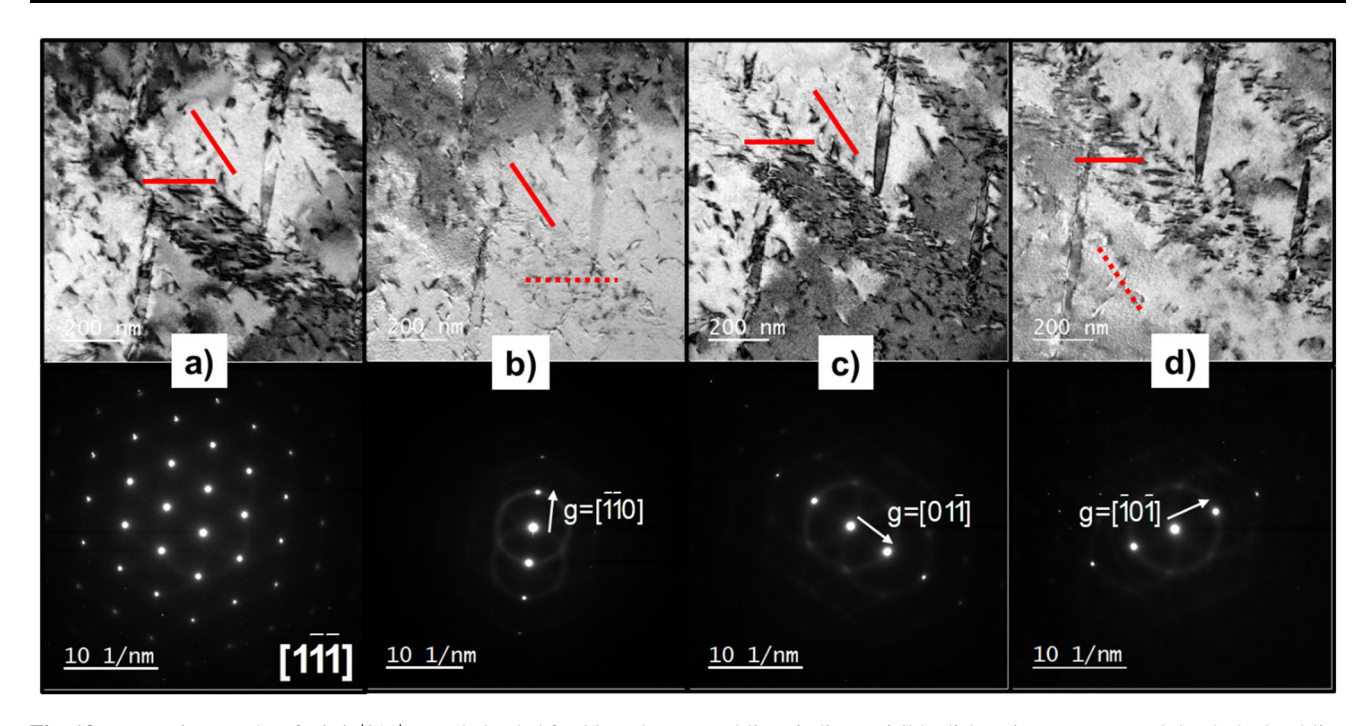


Fig. 13 TEM micrographs of NiTi $\langle 011 \rangle$ sample loaded for 20 cycles at 0.01 Hz imaged along $[1\overline{11}]$ zone axis. **a** Bright field image captured on zone condition, **b** image captured with $g = [\overline{110}]$, **c** image captured with $g = [\overline{101}]$ and **d** image captured with $g = [\overline{101}]$. Solid

red lines indicate visible dislocation contrast, and the dashed red line indicates dislocation invisibility. The g.b analysis revealed that the slip plane belongs to $\{\ 110\}$ and the slip direction is either $\langle 001\rangle$ or $\langle 1\overline{1}1\rangle$ (Color figure online)

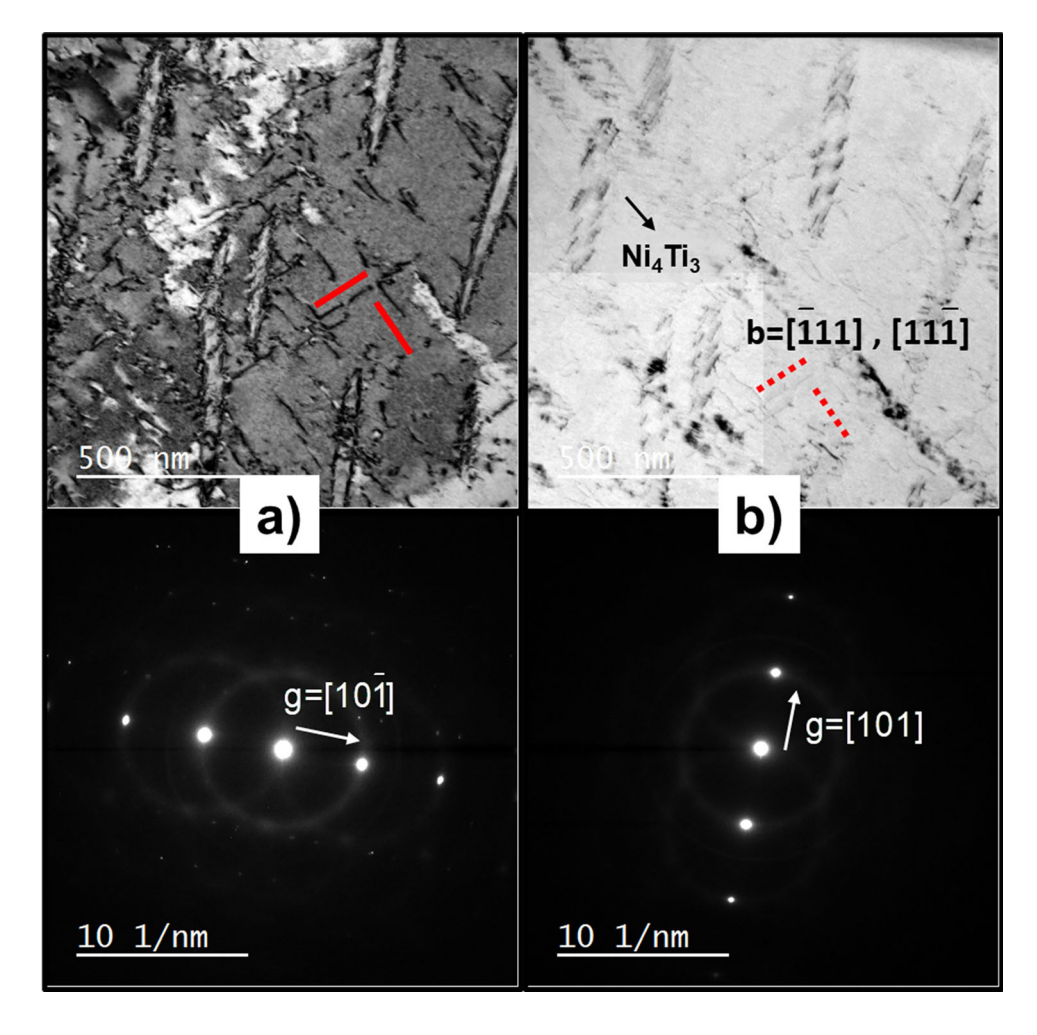
plane $(\overline{11}1)_M$ is parallel to the B2 slip plane $(\overline{11}0)_A$ and the twinning shear direction $(0.5404\ 0.45961)_M$ is nearly parallel to the B2 slip direction $(\overline{1}11)_A$. Hence, depending on which martensite correspondent variant pair (CVP) is activated, during the reverse motion of the A-M interface, the twinning dislocations gliding on the internal twin plane could be transformed into planar dislocations on the closest $\langle 001\rangle\{110\}$ or $\langle \overline{1}11\rangle\{110\}$ B2 slip system. At this point it should be noted that the $\langle 001\rangle\{110\}$ is the most energetically favorable B2 slip system followed by $\langle \overline{1}11\rangle\{110\}$ [53]. This could explain the absence of residual strain in the $\langle 001\rangle$ loading orientation as the resolved shear stress on the most energetically favorable system is zero.

Another plausible mechanism proposed by Kajiwara-Kikuchi [33, 34] which was elucidated by molecular dynamics simulations [43] was that the stress concentration due to the pile up of twinning dislocations at the A-M interface during its reverse motion can trigger a dislocation reaction emitting dislocations into the austenite matrix. The twin thickness of martensite dictates the corresponding twinning dislocation density which help accommodate the coherency strains at the A-M interface [54]. Therefore, as the A-M interface moves with the application of load, the local coherency strain at the A-M1 or A-M2 interface (M1 and M2 are the twin related martensite) can increase as either M1 or M2 grows at the expense of the other. At some point this local coherency strain can be large enough to

trigger plastic relaxation at the interface even during the forward motion of the A-M interface. This could be possible as the stresses are higher during the forward loading as pointed out in a phase field crystal plasticity study [45] which also elucidated the plastic relaxation mechanism. However, this needs experimental confirmation and there seems to be no consensus on whether the transformation induced dislocations in the austenite form during forward transformation or reverse transformation or both. In any case, the source of dislocations seems to be linked to the internal twins of the martensite. This claim could be further substantiated by yet another TEM observation shown in Fig. 16a which depicts ladder-like dislocation arrangement. These could be signatures of martensite twins as elucidated in the schematic shown in Fig. 16b. The coherency stress field at the precipitate-B2 interface aids in martensite nucleation [58–60] which consequently spreads into the B2 matrix. Based on the interaction between the precipitate stress field, the externally applied stress field and the consequent resolved shear stress, the most favorable habit plane variant with type I or type II internal twins is nucleated [61]. The precipitate stress field would vary depending on the precipitate variant and ultimately, upon unloading, transformation induced dislocations are left behind on the $\langle \overline{1}11 \rangle \{110\}$ or $\langle 001 \rangle \{110\}$ B2 slip system as observed in this study.



Fig. 14 TEM micrographs of NiTi $\langle 011 \rangle$ sample loaded for 20 cycles at 0.01 Hz imaged along the [010] zone axis. a Clear dislocation contrast is visible under the $g = [10\overline{1}]$ diffraction condition, b dislocations vanish when imaged under the g = [101]. This confirms that the slip direction is $\langle 111 \rangle$



Additionally, in the current TEM analysis, dislocations have been observed to interact with the Ni₄Ti₃ precipitates. In the Ni_{50.8}Ti single crystals used in this study, different variants of Ni₄Ti₃ precipitates arranged on the parallel $\{111\}_{B2}$ planes were observed. Interaction between a mobile A-M interface and the stress field of a precipitate may result in relaxation of coherency strains in the form of dislocations [35, 62]. These dislocations could pile up and transmit into the precipitate matrix (see Fig. 17) as the martensite shrinks during unloading. Under fatigue loading, the recurrent motion of the A-M interface past a precipitate could result in dislocation pile-up at the precipitate-B2 interface and could ultimately activate slip or shear into the rhombohedral precipitate as evidenced in the TEM micrographs presented in Fig. 17. A mechanism like that of slip transmission across grain boundaries may be active in this case as well. Dislocation incorporation inside the precipitate is yet another dissipative mechanism which results in residual strain accumulation and has not been observed before. The exact mechanism of dislocation accommodation in the precipitate is still unclear and needs further work.

Effect of Loading Frequency on Residual Strain Accumulation

Now that it is established that the residual dislocations observed in the reversed austenite matrix stems from the martensite twin boundaries, it is safe to say that the amount of residual strain upon unloading must depend on the transformation volume. As seen in Fig. 11, the residual strain accumulation is lower for higher loading frequencies. Additionally, it was observed that the transformation stress increases with loading frequency and it was tied to the latent heat release during the onset of transformation as discussed in "NiTi (011)" section. Given that the elastic modulus does not depend on the loading frequency, the elastic strain at the onset of transformation must be larger for higher loading frequency. The heat released by the microscopic nuclei of martensite would heat up the surrounding volume of the B2 matrix, elevating its transformation stress and thereby sustaining larger elastic strains. Consequently, for the same applied maximum strain, the amount of superelastic strains, the corresponding transformed volume and the resultant residual strains must be



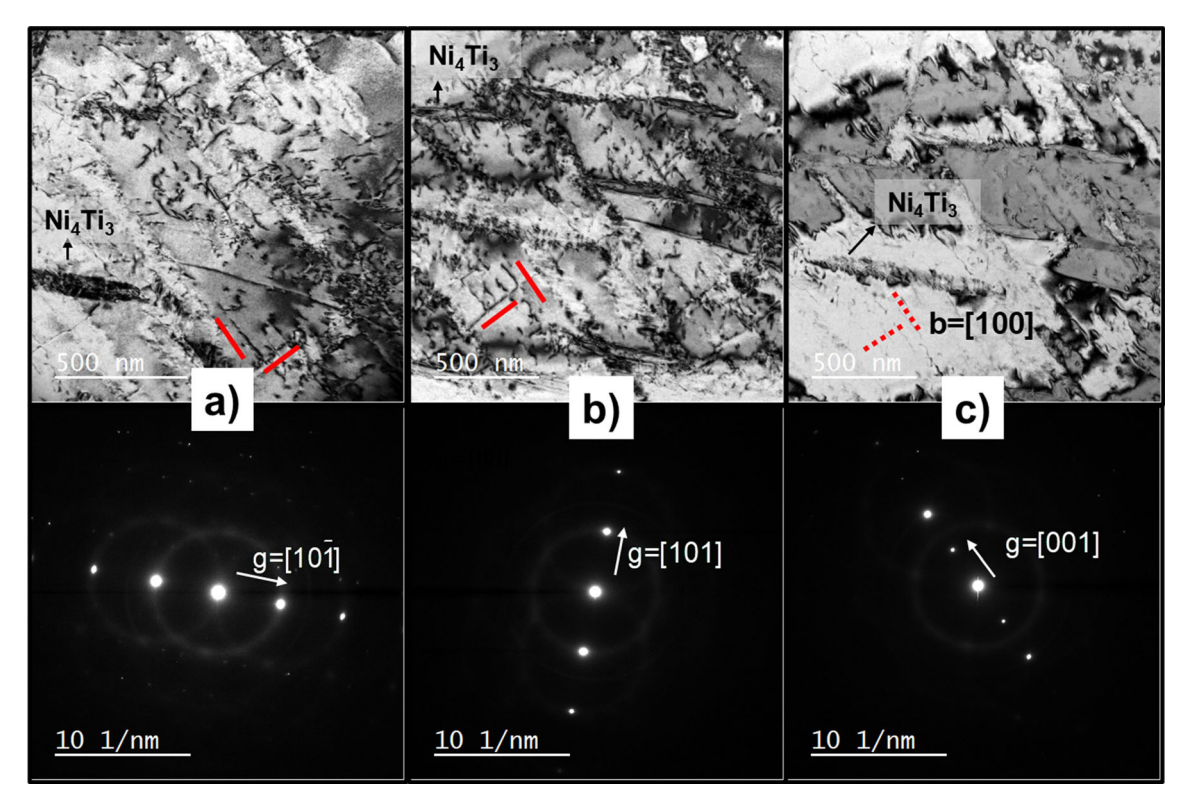


Fig. 15 TEM micrographs of NiTi $\langle 011 \rangle$ sample loaded for 20 cycles at 0.01 Hz imaged along the [010] zone axis. Clear dislocation contrast is visible under the \mathbf{a} $g = [10\overline{1}]$ and \mathbf{b} g = [101] diffraction condition, \mathbf{c} dislocations vanish when imaged under the g = [001]

diffraction. This confirms that the slip direction is $\langle 100 \rangle$. Note that a different region of the same TEM lamella shown in Fig. 14 is depicted in this figure

smaller for larger loading frequencies. This conjecture can be confirmed by looking at isothermal quasi static tests performed on diverse SMAs which exhibit larger elastic strains and smaller hysteresis as the test temperature is increased up to a point [63]. However, the hysteresis widens as $M_{\rm d}$ temperature is approached but heat release during high frequency loading would never reach $M_{\rm d}$ temperatures as NiTi exhibits a superelastic window of operation of around 90 °C [64].

Thermomechanical Concepts

At present, continuum formulations are inherently limited to transformations that occur in a fully reversible manner, and irreversibility is only modeled in a phenomenological manner with a dissipative potential, and in conjunction with the second law of thermodynamics, transformation criterion are developed. At the present, the understanding of the nature of irreversibilities is insufficient to accurately capture them in thermo-mechanical models. These models cannot accurately predict the stress–strain response, the transformation indicators' (i.e. characteristic stresses, etc.) evolution with cycling in cases where unrecoverable strains develop. In our prior work [7], we formulated a continuum

model to explain stress-strain response with loading frequency. Based on a complementary free energy formulation the driving force on a variant n is written as [9, 10],

$$F^{n} = -B(T - T_{0}) + \sum_{ij} \varepsilon_{ij}^{n} + 1/2 \sum_{n} \sigma_{ij}^{m} \varepsilon_{ij}^{n} + \sum_{n} \sigma_{ij}^{p} \varepsilon_{ij}^{n} \quad (1)$$

Transformation proceeds when F^n reaches a critical value F^c . The first term $-B(T-T_0)$ takes into account the chemical free energy difference between austenite and martensite where T is the sample temperature, T_0 is the equilibrium temperature and B is the entropy change during the transformation. The other three terms are non-chemical contributions. The second term represent the external stress and transformation strain interaction on the nth variant. The third term incorporates the martensite stress on the nth variant which can be determined from Eshelby's inclusion principle [10]. The last term takes into account the stresses due to precipitate [61, 65]. When the material is in the parent state, the first and third terms oppose the transformation while the second and fourth term favor the transformation.

As schematically shown in Fig. 1, hysteresis is affected by (i) the temperature transients of the A-M interface, (ii) transformation induced dislocations that are not reversible during the load/unload cycle, and (iii) energy dissipated



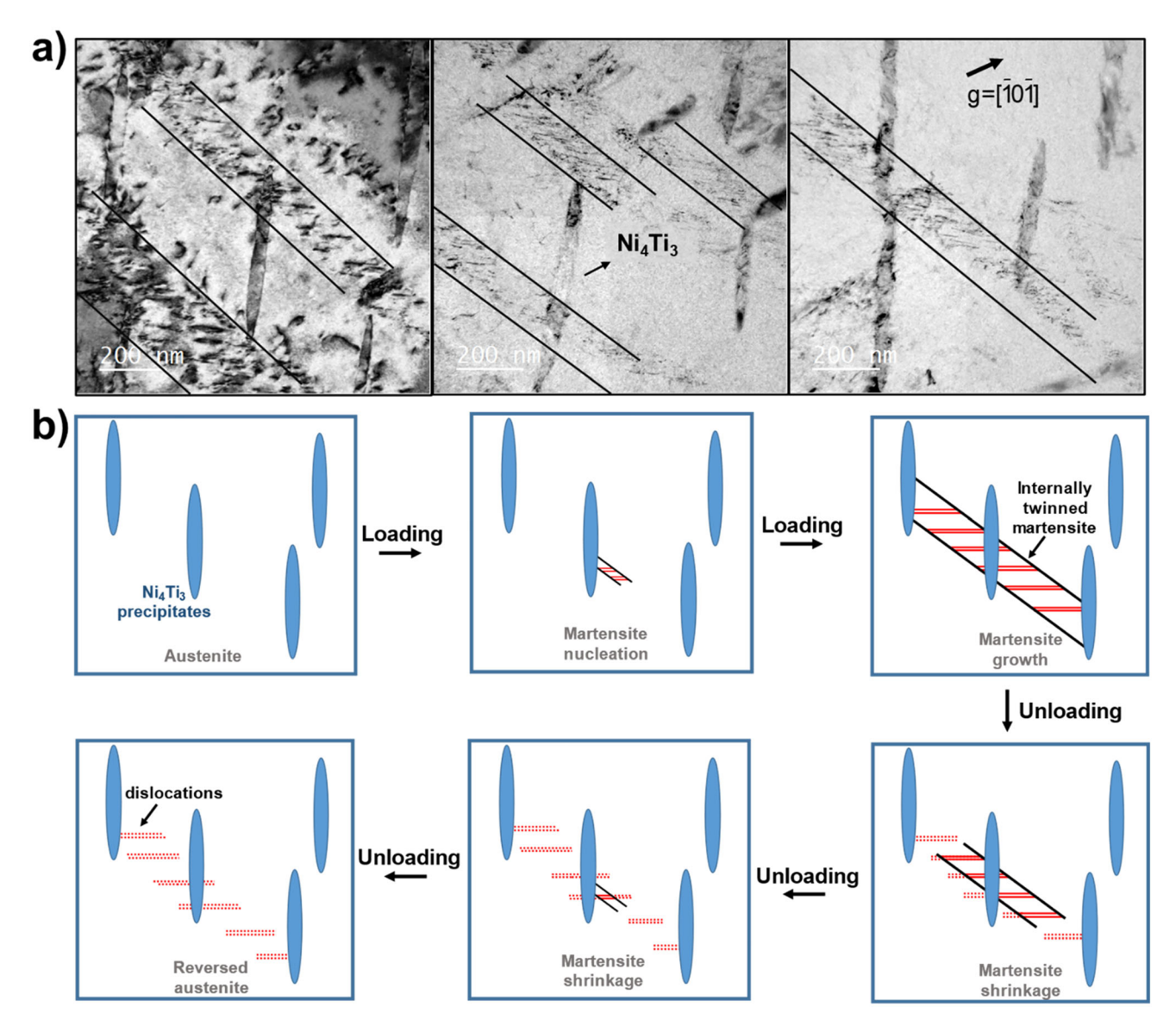


Fig. 16 a TEM observations of the ladder-like dislocation arrangement indicating signatures of martensitic twins. **b** Schematic elucidating the mechanism. During loading martensite nucleates at the precipitate matrix interface [58–60] spreads into the austenitic

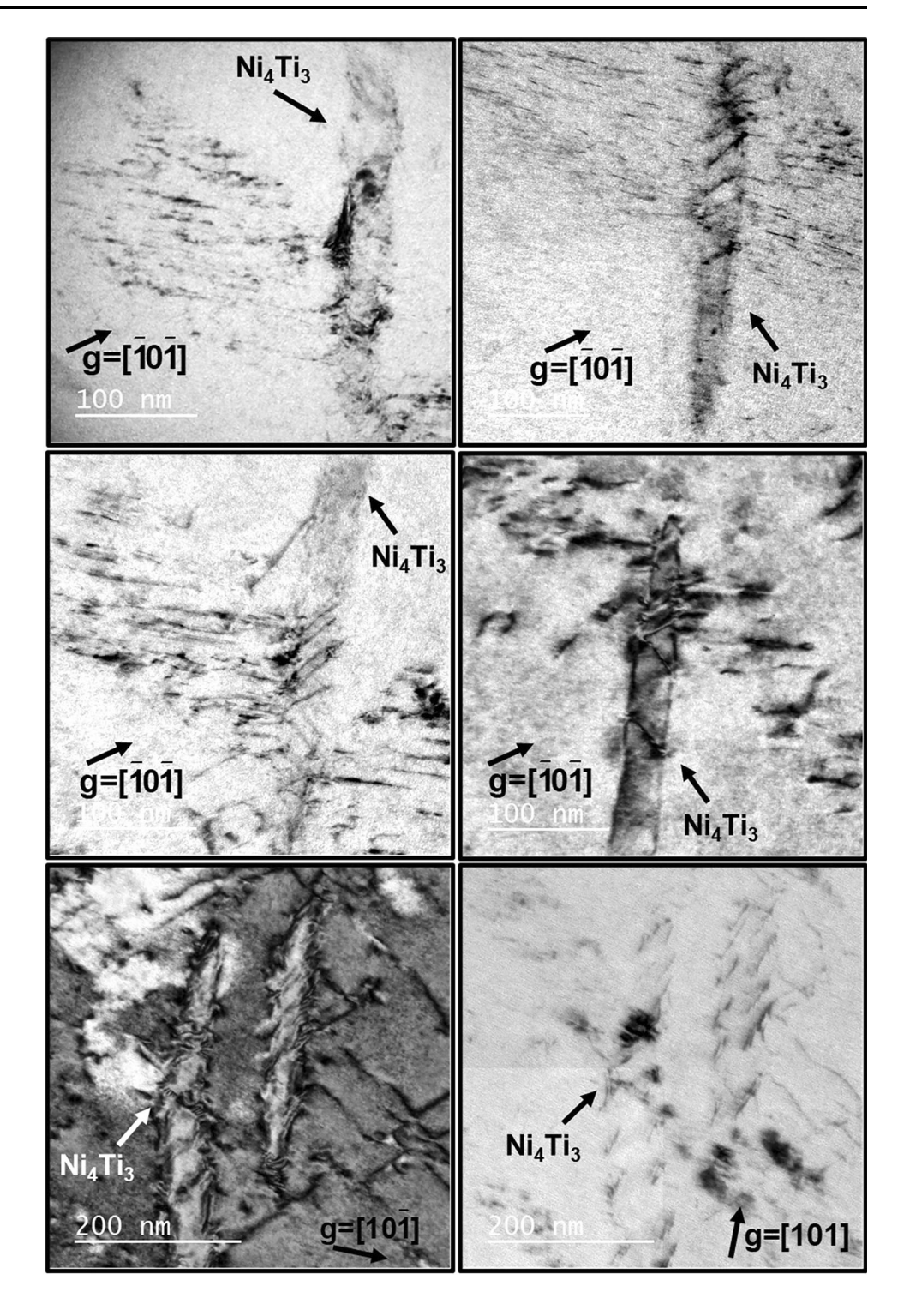
domains in the channels between the precipitates. During unloading, as the martensite shrinks, the twinning dislocations transform into slip dislocations on the closest B2 slip systems dictated by the lattice correspondence

due to the motion of the internal twin interfaces of the martensite. To address (i), our previous modeling efforts [7] captured the reduction in hysteresis with increasing loading frequency in the 0.01 Hz to 10 Hz range due to the transitory effects. Addressing (ii) and (iii) is far more complicated, and beyond the scope of the present study. Suffice it to state that transformation induced plasticity alters the transformation strain term and the martensite stress term (2nd, 3rd and 4th terms) in Eq. (1). In addition, during reverse loading the magnitude of these terms also differ, directly affecting the stress response. Additionally, the TEM analysis reveals that the transformation induced dislocations interact with the precipitates, pile-up along the

precipitate-B2 interface and shear into the precipitate (Fig. 17). The precipitates will assist the forward transformation [61, 65] while resisting the reverse transformation. Finally, in reversible continuum formulations, the value of F^c (or the CRSS for transformation) is the same for forward and reverse transformations. However, the driving forces are substantially altered upon reverse transformation due to the slip contributions. The magnitude of F^c needs to be determined from atomistic consideration incorporating the twin migration energy, GPFE [66] and the phase boundary energy barrier (B2 to B19') [67, 68]. Previous work on the core-spreading of transformation dislocations showed Non-Schmid behavior which suggest a



Fig. 17 Interaction between parallel dislocations and Ni₄Ti₃ precipitate. Dislocation pile-up at the precipitate-B2 interface and dislocations shearing into the precipitate can be clearly evidenced in a–f. All the TEM images were taken from 0.01 Hz sample cycled 20 times



different value of F^c upon forward versus reverse transformation [68]. Furthermore, the slip resistance of parent phase differs in forward versus reverse directions as well [69], therefore the underlying factors contributing to stress hysteresis are rather complex.

Conclusions

The current study supports the following conclusions:

Normalized hysteresis i.e. the specific damping capacity of NiTi (011) and (001) single crystals decrease with increasing loading frequency. Under fatigue loading, this leads to smaller residual strain



- accumulation and better functionality at higher loading frequencies especially for $\langle 011 \rangle$.
- 2. Upon cycling, the normalized hysteresis, the elastocaloric temperature change ($\Delta T_{\rm rev}$) stays constant for $\langle 001 \rangle$ whereas, for $\langle 011 \rangle$, it decreases and stabilizes after cycle 10. Concomitantly the residual strain accumulation increases and stabilizes after cycle 10 for $\langle 011 \rangle$ whereas there is no residual strain accumulation for $\langle 001 \rangle$.
- 3. The forward/reverse transformation stress levels increase with loading frequency for $\langle 001 \rangle$ and $\langle 011 \rangle$. This can be attributed to the self-heating due to the latent heat release/absorption. The $\Delta T_{\rm tr}$ measured at 0.1% strain-offset transformation stress is around 0.4 to 1 °C for 0.01 Hz and reaches as high as 10 °C for 10 Hz loading frequency explaining the amplification of the 0.1% strain-offset transformation stress.
- 4. On the other hand, the forward/reverse transformation stress levels remain unchanged for $\langle 001 \rangle$ and reduces for $\langle 011 \rangle$ upon fatiguing. This is attributable to the transformation induced dislocations which, in the subsequent cycles, lead to the reduction in the total volume of transformation, reduction in ΔT during loading/unloading and generate an internal stress field, all of which reduce the forward/reverse transformation stresses.
- 5. TEM analysis uncovered parallel dislocations on the $\langle 100 \rangle \{ 011 \}_{B2}$ and $\langle \overline{1}11 \rangle \{ 110 \}_{B2}$ austenite slip systems. Based on the lattice correspondences between the austenite and martensite, the source of these dislocations is traced to the type II or type I internal twins, respectively. The CVP with these internal twins is influenced by the local stress fields created by the precipitate variant. This has important implications in understanding martensite deformation.
- Dislocation pile-up and shearing across the precipitate-B2 interface was observed and seems to influence the residual strain accumulation in NiTi SMAs.

Acknowledgments This work is supported by the National Science Foundation Grant DMR- 2104971, Metallic Materials and Nanomaterials Program, which is gratefully acknowledged. SEM, FIB, TEM and EBSD were carried out in part in the Frederick Seitz Materials Research Laboratory Central Research Facilities, University of Illinois Urbana-Champaign.

References

- Lagoudas DC (2008) Shape memory alloys: modeling and engineering applications. Springer, New York
- 2. Hartl DJ, Lagoudas DC (2007) Aerospace applications of shape memory alloys. Proc Inst Mech Eng Part G 221(4):535–552
- 3. Safranski D, Dupont K, Gall K (2020) Pseudoelastic NiTiNOL in orthopaedic applications. Shape Mem Superelast 6(3):332–341

- Duerig TW (2002) The use of superelasticity in modern medicine. MRS Bull 27(2):101–104
- Williams EA, Shaw G, Elahinia M (2010) Control of an automotive shape memory alloy mirror actuator. Mechatronics 20(5):527–534
- Humbeeck JV, Kustov S (2005) Active and passive damping of noise and vibrations through shape memory alloys: applications and mechanisms. Smart Mater Struct 14(5):S171–S185
- Sidharth R, Mohammed A, Abuzaid W, Sehitoglu H (2021) Unraveling frequency effects in shape memory alloys: NiTi and FeMnAlNi. Shape Mem Superelast 7(2):235–249
- Abuzaid W, Wu Y, Sidharth R, Brenne F, Alkan S, Vollmer M, Krooß P, Niendorf T, Sehitoglu H (2019) FeMnNiAl iron-based shape memory alloy: promises and challenges. Shape Mem Superelast 5(3):263–277
- Patoor E, El Amrani M, Eberhardt A, Berveiller M (1995)
 Determination of the origin for the dissymmetry observed
 between tensile and compression tests on shape memory alloys.
 Le Journal de Physique IV 5(C2):C2-495-C2-500
- Gall K, Sehitoglu H (1999) The role of texture in tension-compression asymmetry in polycrystalline NiTi. Int J Plast 15(1):69-92
- Van Humbeeck J (2001) 5.3 The martensitic transformation. In: Materials Science Forum, vol 366–368, pp 382–415
- San Juan J, Nó M (2003) Damping behavior during martensitic transformation in shape memory alloys. J Alloys Compds 355(1–2):65–71
- Blanter MS, Golovin IS, Neuhäuser H, Sinning H-R (2007) Other mechanisms of internal friction, internal friction in metallic materials: a handbook. Springer, Berlin, pp 121–155
- Van Humbeeck J, Delaey L (1981) The influence of strain-rate, amplitude and temperature on the hysteresis of a pseudoelastic Cu-Zn-Al single crystal. J. Phys. Colloques 42(C5):C5-1007-C5-1011
- Van Humbeeck J (2003) Damping capacity of thermoelastic martensite in shape memory alloys. J Alloy Compd 355(1):58–64
- Shaw JA, Kyriakides S (1995) Thermomechanical aspects of NiTi. J Mech Phys Solids 43(8):1243–1281
- 17. He YJ, Sun QP (2011) Rate-dependent damping capacity of NiTi shape memory alloy. Solid State Phenom 172–174:37–42
- He Y, Yin H, Zhou R, Sun Q (2010) Ambient effect on damping peak of NiTi shape memory alloy. Mater Lett 64(13):1483–1486
- He YJ, Sun QP (2011) On non-monotonic rate dependence of stress hysteresis of superelastic shape memory alloy bars. Int J Solids Struct 48(11):1688–1695
- Nemat-Nasser S, Yong Choi J, Guo W-G, Isaacs JB, Taya M (2005) High strain-rate, small strain response of a NiTi shapememory alloy. J Eng Mater Technol 127(1):83–89
- Dayananda GN, Rao MS (2008) Effect of strain rate on properties of superelastic NiTi thin wires. Mater Sci Eng A 486(1):96–103
- Tobushi H, Shimeno Y, Hachisuka T, Tanaka K (1998) Influence of strain rate on superelastic properties of TiNi shape memory allov. Mech Mater 30(2):141–150
- Wolons D, Gandhi F, Malovrh B (1998) Experimental investigation of the pseudoelastic hysteresis damping characteristics of shape memory alloy wires. J Intell Mater Syst Struct 9(2):116–126
- Moumni Z, Herpen AV, Riberty P (2005) Fatigue analysis of shape memory alloys: energy approach. Smart Mater Struct 14(5):S287–S292
- Zhang Y, Moumni Z, You Y, Zhang W, Zhu J, Anlas G (2019) Multiscale TRIP-based investigation of low-cycle fatigue of polycrystalline NiTi shape memory alloys. Int J Plast 115:307–329



- Zhang Y, You Y, Moumni Z, Anlas G, Zhu J, Zhang W (2017)
 Experimental and theoretical investigation of the frequency effect on low cycle fatigue of shape memory alloys. Int J Plast 90:1–30
- 27. Sangid MD, Maier HJ, Sehitoglu H (2011) A physically based fatigue model for prediction of crack initiation from persistent slip bands in polycrystals. Acta Mater 59(1):328–341
- Sangid MD, Maier HJ, Sehitoglu H (2011) An energy-based microstructure model to account for fatigue scatter in polycrystals. J Mech Phys Solids 59(3):595–609
- Sidharth R, Abuzaid W, Sehitoglu H (2020) Nano-twinning enhanced room temperature fatigue crack growth in single crystalline CoCrFeMnNi high entropy alloy. Intermetallics 126:106919
- Sidharth R, Wu Y, Brenne F, Abuzaid W, Sehitoglu H (2020) Relationship between functional fatigue and structural fatigue of iron-based shape memory alloy FeMnNiAl. Shape Mem Superelast 6(2):256–272
- Sidharth R, Abuzaid W, Vollmer M, Niendorf T, Sehitoglu H (2020) Fatigue crack initiation in the iron-based shape memory alloy FeMnAlNiTi. Shape Mem Superelast 6(3):323–331
- Kajiwara S (1999) Characteristic features of shape memory effect and related transformation behavior in Fe-based alloys. Mater Sci Eng A 273–275:67–88
- Kajiwara S, Kikuchi T (1983) Reversible movement of the austenite-martensite interface and dislocation structures in reverse-transformed austenite in Fe-Ni-C alloys. Philos Mag A 48(4):509–526
- Kajiwara S, Kikuchi T (1982) Dislocation structures produced by reverse martensitic transformation in a Cu-Zn alloy. Acta Metall 30(2):589–598
- Hamilton RF, Sehitoglu H, Chumlyakov Y, Maier H (2004)
 Stress dependence of the hysteresis in single crystal NiTi alloys.
 Acta Mater 52(11):3383–3402
- Roy D, Buravalla V, Mangalgiri P, Allegavi S, Ramamurty U (2008) Mechanical characterization of NiTi SMA wires using a dynamic mechanical analyzer. Mater Sci Eng A 494(1-2):429-435
- Norfleet D, Sarosi P, Manchiraju S, Wagner M-X, Uchic M, Anderson P, Mills M (2009) Transformation-induced plasticity during pseudoelastic deformation in Ni–Ti microcrystals. Acta Mater 57(12):3549–3561
- Pelton A, Huang G, Moine P, Sinclair R (2012) Effects of thermal cycling on microstructure and properties in Nitinol. Mater Sci Eng A 532:130–138
- Bowers M, Chen X, De Graef M, Anderson PM, Mills M (2014) Characterization and modeling of defects generated in pseudoelastically deformed NiTi microcrystals. Scripta Mater 78:69–72
- Simon T, Kröger A, Somsen C, Dlouhy A, Eggeler G (2010) On the multiplication of dislocations during martensitic transformations in NiTi shape memory alloys. Acta Mater 58(5):1850–1860
- Delville R, Malard B, Pilch J, Sittner P, Schryvers D (2011) Transmission electron microscopy investigation of dislocation slip during superelastic cycling of Ni–Ti wires. Int J Plast 27(2):282–297
- Ibarra A, San Juan J, Bocanegra E, Nó M (2007) Evolution of microstructure and thermomechanical properties during superelastic compression cycling in Cu–Al–Ni single crystals. Acta Mater 55(14):4789–4798
- Mohammed ASK, Sehitoglu H (2020) Martensitic twin boundary migration as a source of irreversible slip in shape memory alloys. Acta Mater 186:50–67
- 44. Paranjape HM, Manchiraju S, Anderson PM (2016) A phase field-finite element approach to model the interaction between phase transformations and plasticity in shape memory alloys. Int J Plast 80:1–18

- Paranjape HM, Bowers ML, Mills MJ, Anderson PM (2017) Mechanisms for phase transformation induced slip in shape memory alloy micro-crystals. Acta Mater 132:444–454
- Hua P, Chu K, Ren F, Sun Q (2020) Cyclic phase transformation behavior of nanocrystalline NiTi at microscale. Acta Mater 185:507–517
- Gall K, Maier H (2002) Cyclic deformation mechanisms in precipitated NiTi shape memory alloys. Acta Mater 50(18):4643–4657
- Wagner MF, Nayan N, Ramamurty U (2008) Healing of fatigue damage in NiTi shape memory alloys. J Phys D Appl Phys 41(18):185408
- Miyazaki S, Imai T, Igo Y, Otsuka K (1986) Effect of cyclic deformation on the pseudoelasticity characteristics of Ti-Ni alloys. Metall Trans A 17(1):115–120
- Calvi A (2011) Spacecraft loads analysis, an overview. ESA/ ESTEC
- Torra V, Isalgue A, Lovey FC, Sade M (2015) Shape memory alloys as an effective tool to damp oscillations. J Therm Anal Calorim 119(3):1475–1533
- Ozbulut OE, Hurlebaus S, DesRoches R (2011) Seismic response control using shape memory alloys: a review. J Intell Mater Syst Struct 22(14):1531–1549
- 53. Ezaz T, Wang J, Sehitoglu H, Maier H (2013) Plastic deformation of NiTi shape memory alloys. Acta Mater 61(1):67–78
- Kajiwara S, Owen WS (1977) The martensite-austenite interface and the thickness of twins in martensite in Fe3Pt. Scr Metall 11(2):137–142
- Knowles K, Smith D (1981) The crystallography of the martensitic transformation in equiatomic nickel-titanium. Acta Metall 29(1):101–110
- Mohammed ASK, Sehitoglu H (2020) Modeling the interface structure of type II twin boundary in B19' NiTi from an atomistic and topological standpoint. Acta Mater 183:93–109
- 57. Zhang X, Sehitoglu H (2004) Crystallography of the B2→ R→ B19' phase transformations in NiTi. Mater Sci Eng A 374(1-2):292-302
- Bataillard L, Bidaux J-E, Gotthardt R (1998) Interaction between microstructure and multiple-step transformation in binary NiTi alloys using in-situ transmission electron microscopy observations. Philos Mag A 78(2):327–344
- Michutta J, Somsen C, Yawny A, Dlouhy A, Eggeler G (2006)
 Elementary martensitic transformation processes in Ni-rich NiTi single crystals with Ni4Ti3 precipitates. Acta Mater 54(13):3525–3542
- Manchuraju S, Kroeger A, Somsen C, Dlouhy A, Eggeler G, Sarosi P, Anderson P, Mills M (2012) Pseudoelastic deformation and size effects during in situ transmission electron microscopy tensile testing of NiTi. Acta Mater 60(6–7):2770–2777
- 61. Gall K, Sehitoglu H, Chumlyakov YI, Kireeva IV, Maier HJ (1999) The influence of aging on critical transformation stress levels and martensite start temperatures in NiTi: part I—aged microstructure and micro-mechanical modeling
- 62. Hornbogen E (1985) The effect of variables on martensitic transformation temperatures. Acta Metall 33(4):595–601
- 63. Wu Y, Ertekin E, Sehitoglu H (2017) Elastocaloric cooling capacity of shape memory alloys—role of deformation temperatures, mechanical cycling, stress hysteresis and inhomogeneity of transformation. Acta Mater 135:158–176
- Sehitoglu H, Karaman I, Anderson R, Zhang X, Gall K, Maier H, Chumlyakov Y (2000) Compressive response of NiTi single crystals. Acta Mater 48(13):3311–3326
- Chowdhury P, Patriarca L, Ren G, Sehitoglu H (2016) Molecular dynamics modeling of NiTi superelasticity in presence of nanoprecipitates. Int J Plast 81:152–167



- Wang J, Sehitoglu H (2013) Twinning stress in shape memory alloys: theory and experiments. Acta Mater 61(18):6790–6801
- Wang J, Sehitoglu H (2012) Resolving quandaries surrounding NiTi. Appl Phys Lett 101(8):081907
- 68. Alkan S, Sehitoglu H (2019) Prediction of transformation stresses in NiTi shape memory alloy. Acta Mater 175:182–195
- Alkan S, Sehitoglu H (2017) Dislocation core effects on slip response of NiTi- a key to understanding shape memory. Int J Plast 97:126–144

Publisher's Note Springer Nature remains neutral with regard to jurisdictional claims in published maps and institutional affiliations.

